Self-induced splitting of x-ray emission lines

Š. Krušič,[1,2] A. Mihelič,[1] K. Bučar,[1] and M. Žitnik[1]
[1]*Jožef Stefan Institute, Jamova cesta 39, 1000 Ljubljana, Slovenia*
[2]*Faculty of Mathematics and Physics, University of Ljubljana, Jadranska 19, 1000 Ljubljana, Slovenia*

(Received 17 March 2020; revised 18 May 2020; accepted 29 May 2020; published 2 July 2020)

We present a theoretical approach for describing collective x-ray emission processes in extended multilevel targets, based on a combination of propagation equations for the quantum correlation functions and the semiclassical Maxwell-Bloch equations. Such a description overcomes the key deficiencies of the two constituent sets of equations, which have until now been independently used to describe these phenomena. The model developed is employed to study the spectral properties of superfluorescence of $K\alpha$ emission in zinc at ∼8630 eV after inner-shell photoionization with intense attosecond free-electron laser pulses. At high pump intensities, the numerical simulations predict a splitting of the $K\alpha_1$ emission line due to a self-induced Autler-Townes effect, which could readily be observed with standard high-resolution x-ray spectrometers. As short duration of the pump pulse is one of the crucial parameters for the manifestation of this phenomenon in the hard-x-ray regime, experimental verification could be possible due to the most recent developments of free-electron laser sources.

DOI: 10.1103/PhysRevA.102.013102

I. INTRODUCTION

Amplified spontaneous emission (ASE) [1,2] and superfluorescence (SF) [3] are two examples of nonlinear phenomena in light-matter interaction, which have been extensively studied in the optical regime [4–7]. In such setups, the target is typically excited by a short intense light pulse creating an inverted population, and fluorescence to a lower-lying state is observed. The characteristic features of the two phenomena allow for a clear distinction in experimental spectra. In ASE, the number of emitted photons increases exponentially with excited-state density and the duration of the emitted pulse is increased. In contrast, SF exhibits a linear dependence of the number of emitted photons and the emitted pulse is delayed in time with respect to pumping and its duration is decreased [8]. In the optical regime, it is thus possible to observe these phenomena by either detecting the total photon yield or recording the time dependence of the emitted radiation intensity as a function of pump intensity [9,10]. However, the transition between the two regimes is not sharp [11]; increasing the excited-state population in the target leads to the saturation of amplified spontaneous emission, where the emitted field exhibits the characteristics of SF. Due to this, both collective emission processes are often called superfluorescence [12]. This is not to be confused with the term superradiance, as coined by Dicke [13] to describe the radiation emitted from a system of atoms prepared in a superposition of states by a coherent field.

Experimental observation of these phenomena in the x-ray domain has only recently become possible with the development of free-electron lasers (FELs) [14–16]. The high intensity and short duration of pulses produced by these light sources enables the creation of a population inversion, for example, by inner- or valence-shell photoionization, leading to fluorescence in the x-ray or XUV spectral regions, respectively. In this way, ASE has been observed in neon gas [17] and copper foil [18]. In both cases, the amplification of $K\alpha$ emission was observed after ionization of a $1s$ electron by FEL pulses, and the characteristic exponential dependence of the number of emitted photons on the FEL intensity was reported.

Detecting the time dependence of the emitted radiation intensity is not feasible in the x-ray domain because the duration of the emitted pulses is on the order of the excited-state lifetime, which for core-hole states is well below 1 ps [19]. The characteristic features of collective emission are however also manifested in the spectral domain. Spectral features of x-ray superfluorescence have recently been observed in manganese complexes [20] and xenon [21]. In both cases, a broadening of the spectral lines was observed when reaching saturation. The modification of the emission line shape was also observed in several theoretical studies, which additionally predicted the emission line to split into two (or more) peaks when the field intensities become high enough [22,23]. In the UV and x-ray domain, the splitting produced by the Autler-Townes effect and the subsequent induced transparency has been observed by coupling short-lived states with an intense optical laser [24,25]. However, observation of the self-induced Autler-Townes (or AC Stark) splitting of the emission line as predicted for superfluorescence in the x-ray domain is lacking.

Even though theoretical models are capable of reproducing the characteristic features of collective emission processes, quantitative agreement with the experimental results is usually obtained by varying the target parameters, such as target density and length. Since superfluorescence develops from spontaneous emission, a successful model must describe both the quantum field fluctuations in the absence of external electric fields and the interaction of strong electric fields with matter and their propagation through an excited medium in the nonlinear regime [3]. In the past, several different attempts have been made to simulate the evolution of superfluorescence

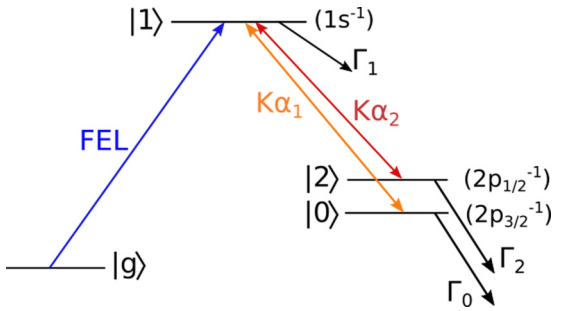

FIG. 1. Schematic representation of the processes after photoionization of a $1s$ electron by a short FEL pulse. The excited state $|1s^{-1}\rangle$ can decay radiatively to states $|2p_{3/2}^{-1}\rangle$ and $|2p_{1/2}^{-1}\rangle$. The three ionic states can further be photoionized or decay nonradiatively to Zn^{2+}.

in different setups, all relying on specific approximations. The most widely used model is based on Maxwell-Bloch equations with spontaneous emission described by a stochastic noise term simulating fluctuations of quantum polarization [26–28]. Such a noise model however does not generate the expected exponentially decreasing emission intensity, but instead produces a temporal profile of the emitted field with a delayed peak with respect to pumping [8], making it inadequate when dealing with multilevel systems and competing decay channels. Recently, a method based on quantum correlation functions has been demonstrated to properly describe both spontaneous and stimulated emission in a two-level system [29]. The model encompasses the transition from spontaneous emission through amplification to superfluorescence and incorporates incoherent processes which are significant in the x-ray regime.

In this paper we extend the approach to modeling collective x-ray emission processes in three-level extended targets, using a combination of quantum correlation functions [29] and Maxwell-Bloch equations [8]. As we will demonstrate, due to the approximations that have to be made to obtain a closed system of propagation equations for the quantum correlation functions, this model is in itself unsuitable to treat nonlinear phenomena in multilevel systems. However, coupling it to the semiclassical Maxwell-Bloch equations enables adequate modeling of both spontaneous emission and effects due to strong electric fields.

The presented model is employed to study the spectral properties of superfluorescence of the $K\alpha_{1,2}$ emission in zinc at ∼8630 eV [30]. The target is photoionized by high-intensity 9750-eV FEL pulses with a duration of a few hundred attoseconds. This has recently become feasible with the demonstration of single-spike self-amplified spontaneous emission (SASE) FEL pulses in both the hard- and soft-x-ray regions [31–33]. In this way, a high density of $1s^{-1}$ excited states is created (Fig. 1). This state can decay via the Auger process, or radiatively to states $2p_{1/2}^{-1}$ and $2p_{3/2}^{-1}$. Other incoherent processes, such as pumping to the lower states and additional photoionization by both the pump and emitted fields, are also taken into account. This target was chosen because of the large energy separation between the two $K\alpha$ lines (23 eV) with respect to their linewidths (∼1 eV), enabling the treatment of the two emission lines by two distinct field modes. Moreover, the lifetime of state $1s^{-1}$ of ∼0.5 fs is longer than the shortest achievable duration of the FEL pulses, which as we will show is required for a clear manifestation of superfluorescence, and the closed d shell in zinc simplifies the treatment of the atomic properties of the target.

II. THEORETICAL DESCRIPTION

We consider an ensemble of atoms, each of which can be represented as a three-level system of Zn^+. This is feasible since we are studying the amplification of two electromagnetic fields resonant with specific radiative transitions proceeding from a common upper level. Each of the levels is degenerate; however, the analysis performed in Appendix A shows that both the magnetic substructure of the ionic levels and polarization properties of the emitted light do not need to be considered explicitly. Since each of the two excited ionic states is initially equally populated and contributes an equal number of photons to each of the two polarization modes in the forward direction, the $K\alpha_1$ and $K\alpha_2$ lines can be treated as resulting from the transition between a single initial state and a final state, the populations of which should be considered as the sum of the populations of the corresponding physical states over the magnetic quantum numbers.

The ionic states are populated as a result of incoherent pumping by a short intense FEL pulse (Fig. 1), which can also lead to valence-shell excitations and shake processes. These most likely result in the production of a $3d$ spectator hole that can subsequently decay by emission of photons with energies in the range of $K\alpha$ emission. For zinc the relative contribution of these processes to the $K\alpha$ emission line intensity is around 10% [34]. According to calculations with the GRASP code [35], the most probable alternative radiative decay process of the $1s$ hole in Zn is $K\beta$ emission involving an electron jump from the $3p$ orbital that has a 12% probability to occur. However, both valence excitation and these additional dipole emission channels cannot be incorporated into the presented model in a straightforward way and are thus neglected, presenting a limitation of this theoretical approach. Higher allowed multipole transitions can be neglected, since the most probable of these is the magnetic dipole transition $|1s_{1/2}^{-1}\rangle \rightarrow |2s_{1/2}^{-1}\rangle$, which in Zn has a probability that is six orders of magnitude lower than that for $K\alpha$ emission.

To simplify the initial treatment of the problem, we assume that all atoms at position z in the target are in the excited state $|1\rangle$ at time $t = z/c$, which corresponds to instantaneous swept-gain pumping of the system, and no incoherent processes are present. These can straightforwardly be included at a later stage. The excited medium is assumed to have the shape of an elongated cylinder, which is the case typically realized in experiments [3]. The excited state radiatively decays to lower-lying states $|0\rangle$ and $|2\rangle$. The effective Hamiltonian operator which describes the atomic system interacting with quantized electric field modes in the dipole and rotating-wave

approximation is written as [36]

$$\begin{aligned} H = &\sum_{\alpha} E_0 \hat{\sigma}_{00}^{(\alpha)} + \sum_{\alpha} E_1 \hat{\sigma}_{11}^{(\alpha)} + \sum_{\alpha} E_2 \hat{\sigma}_{22}^{(\alpha)} \\ &+ \sum_{\boldsymbol{k},s} \hbar\omega_{\boldsymbol{k}} \hat{a}_{\boldsymbol{k},s}^{\dagger} \hat{a}_{\boldsymbol{k},s} + \sum_{\boldsymbol{q},s} \hbar\omega_{\boldsymbol{q}} \hat{b}_{\boldsymbol{q},s}^{\dagger} \hat{b}_{\boldsymbol{q},s} \\ &+ \sum_{\alpha,\boldsymbol{k},s} \hbar[g_{\boldsymbol{k},s} e^{i\boldsymbol{k}\cdot\boldsymbol{r}_\alpha} \hat{\sigma}_{10}^{(\alpha)} \hat{a}_{\boldsymbol{k},s} + g_{\boldsymbol{k},s}^{*} e^{-i\boldsymbol{k}\cdot\boldsymbol{r}_\alpha} \hat{a}_{\boldsymbol{k},s}^{\dagger} \hat{\sigma}_{01}^{(\alpha)}] \\ &+ \sum_{\alpha,\boldsymbol{q},s} \hbar[d_{\boldsymbol{q},s} e^{i\boldsymbol{q}\cdot\boldsymbol{r}_\alpha} \hat{\sigma}_{12}^{(\alpha)} \hat{b}_{\boldsymbol{q},s} + d_{\boldsymbol{q},s}^{*} e^{-i\boldsymbol{q}\cdot\boldsymbol{r}_\alpha} \hat{b}_{\boldsymbol{q},s}^{\dagger} \hat{\sigma}_{21}^{(\alpha)}]. \end{aligned} \tag{1}$$

Here E_i are the energies of the three states and $\hat{\sigma}_{ij} = |i\rangle\langle j|$, $i, j = 0, 1, 2$, the transition operators between the states. The sum $\sum_\alpha$ runs over the atoms in the target. The creation and annihilation operators $\hat{a}_{\boldsymbol{k},s}$ and $\hat{a}_{\boldsymbol{k},s}^{\dagger}$ ($\hat{b}_{\boldsymbol{q},s}$ and $\hat{b}_{\boldsymbol{q},s}^{\dagger}$) correspond to an electromagnetic field mode with wave vector $\boldsymbol{k}$ ($\boldsymbol{q}$), frequency $\omega_{\boldsymbol{k}}$ ($\omega_{\boldsymbol{q}}$), and polarization s. The positive-frequency parts of the quantized electric fields are defined as

$$\hat{\boldsymbol{\mathcal{E}}}_{0,+}^{(\alpha)}(t) = \sum_{\boldsymbol{k},s} \sqrt{\frac{\hbar\omega_{\boldsymbol{k}}}{2\epsilon_0 V}} \boldsymbol{e}_{\boldsymbol{k},s} \hat{a}_{\boldsymbol{k},s}(t) e^{i\boldsymbol{k}\cdot\boldsymbol{r}_\alpha}, \tag{2a}$$

$$\hat{\boldsymbol{\mathcal{E}}}_{2,+}^{(\alpha)}(t) = \sum_{\boldsymbol{q},s} \sqrt{\frac{\hbar\omega_{\boldsymbol{q}}}{2\epsilon_0 V}} \boldsymbol{e}_{\boldsymbol{q},s} \hat{b}_{\boldsymbol{q},s}(t) e^{i\boldsymbol{q}\cdot\boldsymbol{r}_\alpha}, \tag{2b}$$

where $\boldsymbol{e}_{\boldsymbol{k},s}$ ($\boldsymbol{e}_{\boldsymbol{q},s}$) is the polarization vector and V the quantization volume. The negative-frequency parts of the field operators, $\hat{\boldsymbol{\mathcal{E}}}_{0,-}^{(\alpha)}(t)$ and $\hat{\boldsymbol{\mathcal{E}}}_{2,-}^{(\alpha)}(t)$, are defined as Hermitian conjugates of expressions (2). The vector $\boldsymbol{r}_\alpha$ denotes the position of the atom α, which is coupled to the electromagnetic field modes by the electric dipole interaction described by the coupling

$$g_{\boldsymbol{k},s} = \frac{1}{\hbar}\sqrt{\frac{\hbar\omega_{\boldsymbol{k}}}{2\epsilon_0 V}} \boldsymbol{\mu}_{10} \cdot \boldsymbol{e}_{\boldsymbol{k},s}, \quad \boldsymbol{\mu}_{10} = \langle 1|e_0 \hat{\boldsymbol{r}}|0\rangle, \tag{3a}$$

$$d_{\boldsymbol{q},s} = \frac{1}{\hbar}\sqrt{\frac{\hbar\omega_{\boldsymbol{q}}}{2\epsilon_0 V}} \boldsymbol{\mu}_{12} \cdot \boldsymbol{e}_{\boldsymbol{q},s}, \quad \boldsymbol{\mu}_{12} = \langle 1|e_0 \hat{\boldsymbol{r}}|2\rangle. \tag{3b}$$

Here $\hat{\boldsymbol{r}} = \sum_i \hat{\boldsymbol{r}}_{i\alpha}$, where $\hat{\boldsymbol{r}}_{i\alpha}$ is the position of an electron relative to the nucleus of the atom α and the sum $\sum_i$ runs over all the electrons in the atom. The dipole approximation is valid for core-shell excitations in the x-ray domain [37], since the core wave function is exponentially decreasing outside the core radius, which is much smaller than the wavelength of the emitted field.

Following the procedure described in Ref. [29] and detailed in Appendix B, we arrive at the propagation equation for the atomic correlation function between states $|0\rangle$ and $|1\rangle$,

$$\begin{aligned} &\frac{\partial}{\partial\tau}\langle\hat{\sigma}_{10}^{(\alpha)}(\tau)\hat{\sigma}_{01}^{(\beta)}(\tau)\rangle \\ &= -(\Gamma_0^{\mathrm{sp}} + \Gamma_2^{\mathrm{sp}})\langle\hat{\sigma}_{10}^{(\alpha)}(\tau)\hat{\sigma}_{01}^{(\beta)}(\tau)\rangle \\ &\quad + \frac{3\Delta o}{16\pi}\Gamma_0^{\mathrm{sp}}\Bigg\{\sum_{\gamma<\alpha}\langle\hat{\sigma}_{10}^{(\gamma)}(\tau)[\hat{\sigma}_{11}^{(\alpha)}(\tau) - \hat{\sigma}_{00}^{(\alpha)}(\tau)]\hat{\sigma}_{01}^{(\beta)}(\tau)\rangle \\ &\quad + \sum_{\gamma<\beta}\langle\hat{\sigma}_{10}^{(\alpha)}(\tau)[\hat{\sigma}_{11}^{(\beta)}(\tau) - \hat{\sigma}_{00}^{(\beta)}(\tau)]\hat{\sigma}_{01}^{(\gamma)}(\tau)\rangle\Bigg\} - \frac{3\Delta o}{16\pi}\Gamma_2^{\mathrm{sp}} \\ &\quad \times\Bigg\{\sum_{\gamma<\beta}\langle\hat{\sigma}_{10}^{(\alpha)}(\tau)\hat{\sigma}_{02}^{(\beta)}(\tau)\hat{\sigma}_{21}^{(\gamma)}(\tau)\rangle \\ &\quad + \sum_{\gamma<\alpha}\langle\hat{\sigma}_{12}^{(\gamma)}(\tau)\hat{\sigma}_{20}^{(\alpha)}(\tau)\hat{\sigma}_{01}^{(\beta)}(\tau)\rangle\Bigg\} + \langle\hat{F}_{10}^{(\alpha)}(\tau)\hat{F}_{01}^{(\beta)}(\tau)\rangle, \end{aligned} \tag{4}$$

and an analogous expression for $\langle\hat{\sigma}_{12}^{(\alpha)}(\tau)\hat{\sigma}_{21}^{(\beta)}(\tau)\rangle$. Here Γ_0^{sp} and Γ_2^{sp} are the spontaneous decay rates from state $|1\rangle$ to states $|0\rangle$ and $|2\rangle$, respectively, $\Delta o = \pi(r/l)^2$ is the solid angle into which the photons are emitted and is defined by the radius r and length l of the target, τ is the retarded time defined for each atom α as $\tau = t - \frac{z_\alpha}{c}$, and $\hat{F}_{ij}^{(\alpha)}(t)$ are the stochastic Langevin terms due to the interaction with the vacuum field. The right-hand side of Eq. (4) contains expectation values of triple operator products, for which propagation equations can be derived in a similar way. These are coupled to expectation values of quartic operators and so on. In order to obtain a closed set of equations, an approximation has to be made at this point. The triple products in the second term of Eq. (4) can be factorized as [29]

$$\begin{aligned} &\langle\hat{\sigma}_{10}^{(\gamma)}(\tau)[\hat{\sigma}_{11}^{(\alpha)}(\tau) - \hat{\sigma}_{00}^{(\alpha)}(\tau)]\hat{\sigma}_{01}^{(\beta)}(\tau)\rangle \\ &\quad \approx [\langle\hat{\sigma}_{11}^{(\alpha)}(\tau)\rangle - \langle\hat{\sigma}_{00}^{(\alpha)}(\tau)\rangle]\langle\hat{\sigma}_{10}^{(\gamma)}(\tau)\hat{\sigma}_{01}^{(\beta)}(\tau)\rangle. \end{aligned} \tag{5}$$

However, the same approximation cannot be made to resolve the third term on the right-hand side of Eq. (4), as the triple products there are composed of all nondiagonal operators $\hat{\sigma}_{ij}$, $i \neq j$. These products include the operators $\hat{\sigma}_{02}$ and $\hat{\sigma}_{20}$ coupling the two lower states of the three-level system, which are not directly dipole coupled by an electric field mode. These contributions can be neglected when neither of the electric fields is too strong (see Appendix B). Applying these approximations and following the remainder of the derivation in Ref. [29], as well as including the incoherent processes, leads to the closed set of equations

$$\begin{aligned} \frac{\partial}{\partial\tau}\rho_{11}(z,\tau) = r_1(z,\tau) - [\Gamma_0^{\mathrm{sp}} + \Gamma_2^{\mathrm{sp}} + \Gamma_1(z,\tau)]\rho_{11}(z,\tau) - \frac{3\Delta o}{8\pi}\Gamma_0^{\mathrm{sp}} n\int_0^z dz' A_0(z,z',\tau)S_0(z,z',\tau) \\ - \frac{3\Delta o}{8\pi}\Gamma_2^{\mathrm{sp}} n\int_0^z dz' A_2(z,z',\tau)S_2(z,z',\tau), \end{aligned} \tag{6a}$$

$$\frac{\partial}{\partial\tau}\rho_{ii}(z,\tau) = r_i(z,\tau) - \Gamma_i(z,\tau)\rho_{ii}(z,\tau) + \Gamma_i^{\mathrm{sp}}\rho_{11}(z,\tau) + \frac{3\Delta o}{8\pi}\Gamma_i^{\mathrm{sp}} n\int_0^z dz' A_i(z,z',\tau)S_i(z,z',\tau), \tag{6b}$$

$$\frac{\partial}{\partial\tau}S_i(z_1,z_2,\tau) = -\frac{1}{2}[\Gamma_{i1}(z_1,\tau)+\Gamma_{i1}(z_2,\tau)]S_i(z_1,z_2,\tau)$$
$$+\frac{3\Delta o}{16\pi}\Gamma_i^{\rm sp}n\Big\{[\rho_{11}(z_1,\tau)-\rho_{ii}(z_1,\tau)]\int_0^{z_1}dz_1'A_i(z_1,z_1',\tau)S_i(z_1',z_2,\tau)$$
$$+[\rho_{11}(z_2,\tau)-\rho_{ii}(z_2,\tau)]\int_0^{z_2}dz_2'A_i(z_2,z_2',\tau)S_i(z_1,z_2',\tau)\Big\}$$
$$+\frac{3\Delta o}{16\pi}\Gamma_i^{\rm sp}\{[\rho_{11}(z_1,\tau)-\rho_{ii}(z_1,\tau)]\rho_{11}(z_2,\tau)A_i(z_1,z_2,\tau)\Theta(z_1-z_2)$$
$$+[\rho_{11}(z_2,\tau)-\rho_{ii}(z_2,\tau)]\rho_{11}(z_1,\tau)A_i(z_2,z_1,\tau)\Theta(z_2-z_1)\}, \tag{6c}$$

$$\frac{\partial}{\partial z}G_i(z,\tau_1,\tau_2) = -\frac{1}{2}[\kappa_i(z,\tau_1)+\kappa_i(z,\tau_2)]G_i(z,\tau_1,\tau_2)+\frac{3\Delta o}{16\pi}\Gamma_i^{\rm sp}n\Big\{\int_0^{\tau_1}d\tau_1'D_{i1}(z,\tau_1,\tau_1')[\rho_{11}(z,\tau_1')-\rho_{ii}(z,\tau_1')]$$
$$\times G_i(z,\tau_1',\tau_2)+\int_0^{\tau_2}d\tau_2'D_{i1}(z,\tau_2,\tau_2')[\rho_{11}(z,\tau_2')-\rho_{ii}(z,\tau_2')]G_i(z,\tau_1,\tau_2')\Big\}$$
$$+\frac{3\hbar\Delta o^2\Omega_{1i}^3}{16^2\pi^3\epsilon_0c^3}\Gamma_i^{\rm sp}n\Big\{D_{i1}(z,\tau_1,0)D_{i1}(z,\tau_2,0)\rho_{11}(z,0)$$
$$+\int_0^{\min(\tau_1,\tau_2)}d\tau' D_{i1}(z,\tau_1,\tau')D_{i1}(z,\tau_2,\tau')[r_1(z,\tau')+\Gamma_i(z,\tau')\rho_{11}(z,\tau')]\Big\}, \tag{6d}$$

where $i=0,2$, Ω_{1i} is the frequency of the transition between states $|1\rangle$ and $|i\rangle$, $n=N\pi r^2$ is the linear atom density (N is the number of atoms per unit volume), and $\Theta(z)$ is the Heaviside function. Here we introduced the continuous variables for the state populations, correlation functions of atomic coherences, and field correlation functions as follows:

$$\rho_{ii}(z,\tau) = \frac{1}{n\Delta z}\sum_{\alpha:z<z_\alpha<z+\Delta z}\langle\hat\sigma_{ii}^{(\alpha)}(\tau)\rangle, \tag{7a}$$

$$S_i(z_1,z_2,\tau) = \frac{1}{(n\Delta z)^2}\sum_{\substack{\alpha:z_1<z_\alpha<z_1+\Delta z\\ \beta:z_2<z_\beta<z_2+\Delta z}}\langle\hat\sigma_{1i}^{(\alpha)}(\tau)\hat\sigma_{i1}^{(\beta)}(\tau)\rangle, \tag{7b}$$

$$G_i(z,\tau_1,\tau_2) = \frac{1}{n\Delta z}\sum_{\alpha:z<z_\alpha<z+\Delta z}\langle\hat{\mathcal{E}}_{i,-}^{(\alpha)}(\tau_1)\hat{\mathcal{E}}_{i,+}^{(\alpha)}(\tau_2)\rangle e^{i\Omega_{1i}(\tau_1-\tau_2)}. \tag{7c}$$

The effect of the incoherent processes is included in rates $r_i(z,t)$ describing incoherent pumping to the three states and their additional decay rates Γ_1 and Γ_i, leading to

$$\Gamma_{i1}(z,\tau) = \Gamma_0^{\rm sp}+\Gamma_2^{\rm sp}+\Gamma_1(z,\tau)+\Gamma_i(z,\tau). \tag{8}$$

We have not included any effects of decoherence or nonradiative decays between the excited and lower states, as they will not be relevant for the description of the problem in Fig. 1, but these can be added in an analogous way. The inclusion of incoherent processes introduces additional absorption and decoherence factors defined as

$$A_i(z_2,z_1,\tau) = \exp\left(-\frac{1}{2}\int_{z_1}^{z_2}dz'\kappa_i(z',\tau)\right), \tag{9a}$$

$$D_{i1}(z,\tau_2,\tau_1) = \exp\left(-\frac{1}{2}\int_{\tau_1}^{\tau_2}d\tau'\Gamma_{i1}(z,\tau')\right), \tag{9b}$$

where κ_i is the absorption coefficient for the field mode $\mathcal{E}_i$. The intensity of the emitted fields can be defined through the field correlation function as $I_i(z,\tau)=G_i(z,\tau,\tau)$ or expressed in terms of the atomic variables as

$$I_i(z,t) = \frac{3\hbar\Delta o^2\Omega_{1i}^3 n}{16^2\pi^3\epsilon_0c^3}\Gamma_i^{\rm sp}\Big\{n\int_0^z dz_1'\int_0^z dz_2'A_i(z,z_1',\tau)$$
$$\times A_i(z,z_2',\tau)S_i(z_1',z_2',\tau)$$
$$+\int_0^z dz'A_i^2(z,z',\tau)\rho_{11}(z',\tau)\Big\}. \tag{10}$$

In the specific case shown in Fig. 1, pumping to the three ionic states starts from the common ground atomic state by photoionization with an external (FEL) pulse. The evolution of the ground-state population ρ_{gg} and intensity of the pump FEL field $I_{\mathcal{P}}$ can thus be expressed as

$$\frac{\partial}{\partial\tau}\rho_{gg}(z,\tau) = -\left[\sum_{i=0,1,2}\tilde r_i(z,\tau)+\tilde r_x(z,\tau)\right]\rho_{gg}(z,\tau), \tag{11a}$$

$$\frac{\partial}{\partial z}I_{\mathcal{P}}(z,\tau) = -\kappa_{\mathcal{P}}(z,\tau)I_{\mathcal{P}}(z,\tau), \tag{11b}$$

where the pumping rates $\tilde r_i$ are connected to the rates defined in Eqs. (6) by $r_i(z,\tau)=\tilde r_i(z,\tau)\rho_{gg}(z,\tau)$ and $\tilde r_x$ is the rate describing pumping to states not encompassed in the three-level system. The absorption coefficient for the pump field is defined as $\kappa_{\mathcal{P}}=N\sum_{i=g,0,1,2}\sigma_{\mathcal{P}i}\rho_{ii}$, where $\sigma_{\mathcal{P}i}$ is the cross section for photoionization of state $|i\rangle$ with the pump field.

The set of equations (6) describes well the evolution of the system in the spontaneous emission limit; however, because the terms containing the operators $\hat\sigma_{02}$ and $\hat\sigma_{02}$ in Eq. (4) and the analogous expression for the atomic correlation function between states $|1\rangle$ and $|2\rangle$ are neglected, it does not describe the system adequately when the number of emitted photons becomes large. Under these conditions, it is however expected

that the contribution of spontaneous emission is negligible, the essential atomic coherences have been built up, and the emitted radiation can be treated classically. The correlation functions can thus be factorized as

$$S_i(z_1, z_2, \tau) = \rho_{i1}(z_1, \tau)\rho_{1i}(z_2, \tau), \tag{12a}$$

$$G_i(z, \tau_1, \tau_2) = \mathcal{E}_{i,-}(z, \tau_1)\mathcal{E}_{i,+}(z, \tau_2), \tag{12b}$$

where ρ_{i1} and ρ_{1i} are the off-diagonal elements of the density matrix and $\mathcal{E}_{i,\pm}$ are the slowly varying amplitudes of the classical electric field modes. In this so-called semiclassical regime, the system is typically described by means of the Maxwell-Bloch equations [38], which can be obtained by replacing the transition and field operators in the Heisenberg equations of motion by complex numbers and neglecting the stochastic Langevin terms (see details in Appendix B). This leads to the set of propagation equations for the density matrix elements and classical electric fields

$$\frac{\partial}{\partial\tau}\rho_{ii}(z,\tau) = r_i(z,\tau) - \Gamma_i(z,\tau)\rho_{ii}(z,\tau) + \Gamma_i^{\rm sp}\rho_{11}(z,\tau) + \frac{i}{\hbar}[\mu_{1i}\rho_{i1}(z,\tau)\mathcal{E}_{i,+}(z,\tau) - \mu_{i1}\rho_{1i}(z,\tau)\mathcal{E}_{i,-}(z,\tau)], \tag{13a}$$

$$\frac{\partial}{\partial\tau}\rho_{11}(z,\tau) = r_1(z,\tau) - [\Gamma_1(z,\tau) + \Gamma_0^{\rm sp} + \Gamma_2^{\rm sp}]\rho_{11}(z,\tau) - \frac{i}{\hbar}[\mu_{10}\rho_{01}(z,\tau)\mathcal{E}_{0,+}(z,\tau) - \mu_{01}\rho_{10}(z,\tau)\mathcal{E}_{0,-}(z,\tau)] - \frac{i}{\hbar}[\mu_{12}\rho_{21}(z,\tau)\mathcal{E}_{2,+}(z,\tau) - \mu_{21}\rho_{12}(z,\tau)\mathcal{E}_{2,-}(z,\tau)], \tag{13b}$$

$$\frac{\partial}{\partial\tau}\rho_{10}(z,\tau) = -\frac{\Gamma_{01}(z,\tau)}{2}\rho_{10}(z,\tau) + \frac{i}{\hbar}[\rho_{11}(z,\tau) - \rho_{00}(z,\tau)]\mu_{10}\mathcal{E}_{0,+}(z,\tau) - \frac{i}{\hbar}\mu_{12}\rho_{20}(z,\tau)\mathcal{E}_{2,+}(z,\tau), \tag{13c}$$

$$\frac{\partial}{\partial\tau}\rho_{12}(z,\tau) = -\frac{\Gamma_{12}(z,\tau)}{2}\rho_{12}(z,\tau) + \frac{i}{\hbar}[\rho_{11}(z,\tau) - \rho_{22}(z,\tau)]\mu_{12}\mathcal{E}_{2,+}(z,\tau) - \frac{i}{\hbar}\mu_{10}\rho_{02}(z,\tau)\mathcal{E}_{0,+}(z,\tau), \tag{13d}$$

$$\frac{\partial}{\partial\tau}\rho_{02}(z,\tau) = -\frac{\Gamma_{02}(z,\tau)}{2}\rho_{02}(z,\tau) + \frac{i}{\hbar}\mu_{12}\rho_{01}(z,\tau)\mathcal{E}_{2,+}(z,\tau) - \frac{i}{\hbar}\mu_{01}\rho_{12}(z,\tau)\mathcal{E}_{0,-}(z,\tau), \tag{13e}$$

$$\frac{\partial}{\partial z}\mathcal{E}_{i,+}(z,\tau) = -\frac{\kappa_i}{2}\mathcal{E}_{i,+}(z,\tau) - i\frac{\Omega_{1i}}{2\epsilon_0 c}\mu_{i1}N\xi_i\rho_{1i}(z,\tau), \tag{13f}$$

where again $i = 0, 2$. The dipole matrix elements are denoted by μ_{ij} and an additional decoherence rate is introduced as

$$\Gamma_{02}(z,\tau) = \Gamma_0(z,\tau) + \Gamma_2(z,\tau). \tag{14}$$

Comparing Eqs. (13) to a set of Maxwell-Bloch equations derived from the classical Maxwell equations and a Hamiltonian coupling the quantized atomic system to a classical electromagnetic field [38], one notices that an additional factor appears in the field propagation equation (13f),

$$\xi_i = \frac{\Delta o \pi r^2}{2\lambda_i^2}, \quad i = 0, 2, \tag{15}$$

in which λ_i is the wavelength of the field emitted on the $1 \to i$ transition. This is a geometrical factor that is a consequence of performing a one-dimensional approximation, where we assume that only the modes of the field with wave vectors oriented along the cylinder axis within a small solid angle Δo will interact with a large number of atoms and thus be amplified. The effect of this factor on the numerical results is negligible if the geometrical solid angle approximately corresponds to the diffraction solid angle $r^2/l^2 \sim \lambda^2/r^2$. This is equivalent to the condition that the Fresnel number $F \sim r^2/l\lambda \sim \sqrt{\xi}$ is on the order of 1, which has been argued to be the only case in which the reduction of the problem to a single spatial dimension is feasible [3]. In targets characterized by a large Fresnel number, the emission is however expected to occur in smaller independent regions defined by the diffraction solid angle. In these cases, the geometrical solid angle should be replaced with the diffraction solid angle $\Delta o \sim (\lambda/r)^2$ in Eqs. (6) to approximately account for the losses due to the diffraction effects, although strictly speaking the evolution of the system should be treated as a three-dimensional problem.

The coupling between the lower-lying states of the three-level system, which has been neglected in the derivation of the correlation-function equations (6), is included in the Maxwell-Bloch equations in Eqs. (13c)–(13e) via the ρ_{02} coherence. Analyzing Eq. (13e) again shows that the contribution of this coupling will be important when the amplitudes of both fields and coherences ρ_{01} and ρ_{21} become large. This makes Maxwell-Bloch equations suitable for describing the evolution of the system in the region of the phase space where the treatment with quantum correlation functions is inadequate. On the other hand, it can be seen that if one assumes an absence of fields and coherences at time $\tau = 0$, none of them will appear at later times due to the propagation of the Maxwell-Bloch equations alone, unless introducing an extra source term.

Since the propagation region where one of the derived models can accurately describe the evolution of the system coincides with the region where the other cannot, one is able to devise a method for coupling the two sets of equations. At short times and propagation distances, spontaneous emission is the process dominating the system evolution, so the starting point of the model is the quantum correlation-function equations (6). The transition to the Maxwell-Bloch equations (13) should be performed if and when the following two conditions are fulfilled: The contribution of spontaneous with respect to stimulated emission is negligible on both transitions and the contribution of the coupling between states $|0\rangle$ and $|2\rangle$ is still not significant. Quantitatively, the first condition can

be expressed as $R_{\mathcal{E}_i} \gg 1$, where $R_{\mathcal{E}_i}$ denotes the ratio of the stimulated and spontaneous emission terms in Eq. (10):

$$R_{\mathcal{E}_i} = \frac{n\int_0^z dz_1' \int_0^z dz_2' A_i(z,z_1',\tau)A_i(z,z_2',\tau)S_i(z_1',z_2',\tau)}{\int_0^z dz' A_i^2(z,z',\tau)\rho_{11}(z',\tau)}. \quad (16)$$

The second condition can be defined in terms of the contributions to the Maxwell-Bloch equations for the coherences ρ_{01} and ρ_{21} whose evolution is described by Eqs. (13c) and (13d). Deriving these directly from the propagation equations (6c) for the atomic correlation functions using the factorization given by Eq. (12) leads to equations similar to Eqs. (13c) and (13d), but without the last term on the right-hand side of each. This is exactly the term describing the coupling between the lower-lying states which was neglected in the derivation of the quantum correlation-function equations. Defining

$$R_0 = \frac{\mu_{12}\rho_{20}(z,\tau)\mathcal{E}_{2,+}(z,\tau)}{[\rho_{11}(z,\tau)-\rho_{00}(z,\tau)]\mu_{10}\mathcal{E}_{0,+}(z,\tau)}, \quad (17a)$$

$$R_2 = \frac{\mu_{10}\rho_{02}(z,\tau)\mathcal{E}_{0,+}(z,\tau)}{[\rho_{11}(z,\tau)-\rho_{22}(z,\tau)]\mu_{12}\mathcal{E}_{2,+}(z,\tau)} \quad (17b)$$

thus leads to the second condition for the transition to the Maxwell-Bloch equations, that is, $R_i \ll 1$ with $i = 0, 2$.

To obtain numerical results, the equations are rewritten in their finite-difference form and propagated on a two-dimensional grid with one spatial dimension. During the propagation of the correlation-function equations (6), the ratios $R_{\mathcal{E}_0}$ and $R_{\mathcal{E}_2}$ are calculated at each grid point. When the values of both ratios exceed a chosen limiting value, the transition to the Maxwell-Bloch equations is performed and the ratios $R_{0,2}$ are calculated to validate the second condition described above. Performing the transition from the correlation-function model to the Maxwell-Bloch equations requires relating the variables used in the two models. This is straightforward for the state populations, as the expected values ρ_{ii} defined in Eqs. (6) directly correspond to the diagonal density matrix elements in Eqs. (13). However, the atomic and field correlation functions are connected to the electric fields and coherences through Eqs. (12). Taking into account the discretization of the propagation grid, the atomic and field correlation functions are represented by two-dimensional real square matrices at each time or position, respectively. From these, the discretized coherences and electric fields can be obtained by means of the singular-value decomposition [39]. As it turns out, with the parameters studied in the following section, this procedure generally yields one singular value much larger than the others. The coherences and fields are then obtained by multiplying the square root of this value by the corresponding basis vector. The arbitrary overall phase of the obtained fields is chosen so that they are real and positive at short times. The structure of the Maxwell-Bloch equations then dictates that the starting points for the coherences ρ_{01} and ρ_{21} have to lie on the positive imaginary axis. As there is no variable analogous to the density matrix element $\rho_{02}(z,\tau)$ in the correlation-function model, this variable is set to zero at the transient region. This leads to real values of the fields and the coherence ρ_{02} and purely imaginary values of the other two coherences throughout the region where the system evolution is described by the Maxwell-Bloch equations.

In addition to the temporal profiles of the emitted fields, emission spectra can also be extracted from the simulation. In the region where the system evolution is described by the quantum correlations functions, the spectral intensity of the emitted fields can be obtained from the Fourier transform of the field correlation functions according to the Wiener-Khinchin theorem. The calculation of spectra is seemingly less straightforward at propagation distances at which the time evolution is partially described by both sets of equations. In such a situation, the contribution to the spectral intensity from spontaneous emission at short times is negligible with respect to the contribution of intensity at longer times, when the fields are amplified. As the amplification and the saturation stage of the field evolution is described by the Maxwell-Bloch equations, the emission spectra are obtained by the Fourier transform of the calculated electric fields.

III. RESULTS AND DISCUSSION

As an example of a problem that can be solved by the model described in the preceding section, we will study collective emission following inner-shell photoionization of zinc with the ground-state configuration $[\mathrm{Ar}]3d^{10}4s^2$ (Fig. 1). The excited state $1s^{-1}$ with a natural width of 1.67 eV [19] decays via the Auger process with a branching ratio of 0.526 [40], or radiatively to states $2p_{3/2}^{-1}$ and $2p_{1/2}^{-1}$ exhibiting 0.72 and 0.65 eV natural widths, respectively [19]. The K-L fluorescence to the lower states proceeds through the $K\alpha_1$ and $K\alpha_2$ channels by emission of 8638.9- and 8615.8-eV photons, respectively, and the corresponding branching ratios are 0.28 and 0.14 [41]. The ionic states $1s_{1/2}^{-1}$, $2p_{3/2}^{-1}$, and $2p_{1/2}^{-1}$ correspond to the states $|1\rangle$, $|0\rangle$, and $|2\rangle$ of the three-level system presented in Fig. 1, respectively (see Appendix A). The photoionization cross sections required for the determination of the incoherent pumping rates, field absorption coefficients, and partial decay rates can be found in Ref. [42], or they can be calculated with the GRASP [35] and RATIP [43] codes. In order to maximize the population transfer to the excited state, the energy of the pump FEL photons is assumed to be 9750 eV, which is right above the zinc K edge at 9659 eV [41].

The shape of the target is determined by the intersection of the pump field with a thin zinc foil. The length of the target equals the foil thickness, which we take to be $l = 5$ μm, and the radius of the emitting cylinder is defined by the cross section of the pump beam. At this point we take the radius to correspond to the condition $F \sim \xi^2 \sim 1$ discussed in the preceding section, which leads to $r \sim (l^2\lambda^2)^{1/4} \approx 28$ nm. We will later generalize the model to approximately account for larger radii corresponding to $F > 1$.

A. Analysis of the developed model

Contrary to the femtosecond hard-x-ray pulses produced by FELs based on SASE, the intensity profile of the recently demonstrated subfemtosecond FEL pulses consists of a single spike [31,32] and can thus be approximated by a Gaussian with a full width at half maximum duration of $\tau_{\mathcal{P}}$, $I_{\mathcal{P}}(0,\tau) = I_0 \exp[-4\ln(2)(\tau-\tau_0)^2/\tau_{\mathcal{P}}^2]$, where τ_0 is the temporal position of the pulse peak and I_0 the peak intensity.

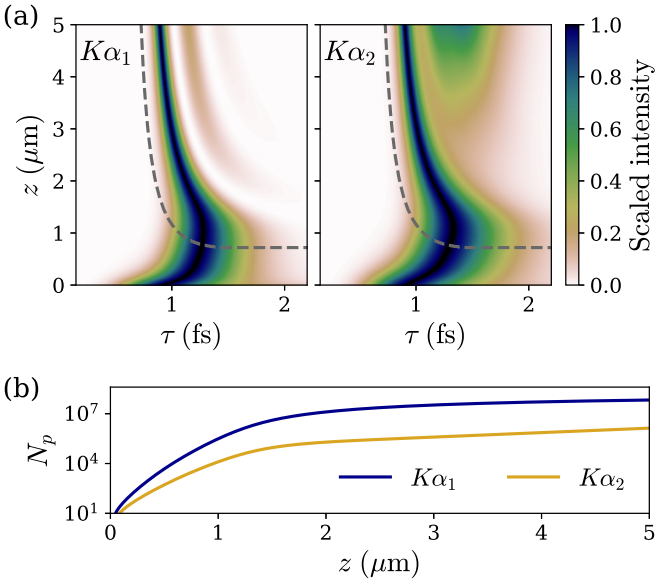

FIG. 2. (a) Intensity of the emitted radiation on the $K\alpha_1$ (left) and $K\alpha_2$ (right) transition normalized to the maximum intensity at each propagation distance z. The dashed lines denote the transition between the two sets of equations. (b) Number of emitted photons as a function of the propagation distance.

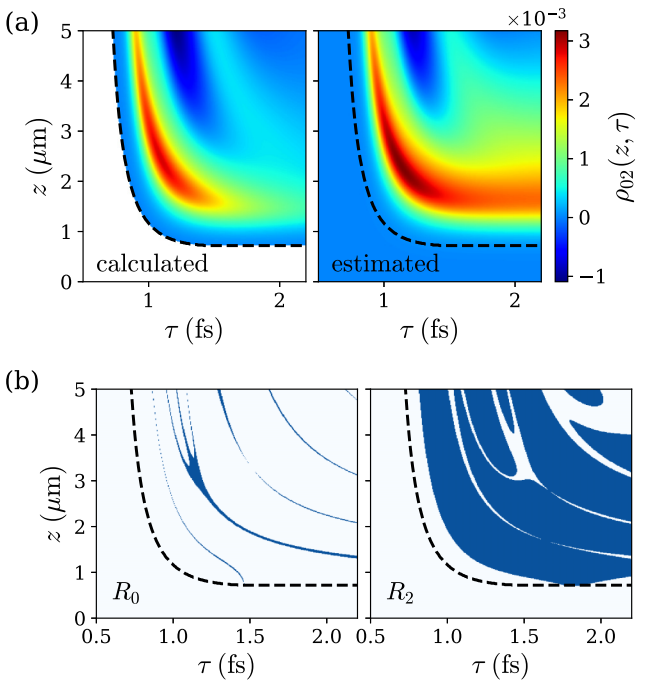

FIG. 3. (a) Calculated (left) and estimated (right; see the text) values of the ρ_{02} density matrix element. (b) Ratios R_0 (left) and R_2 (right). The (dark) blue color shows the regions where the ratios are larger than 0.1. In both plots the dashed lines denote the transition between the two sets of equations.

We assume that the spatial intensity profile of the FEL pulse is uniform inside an area defined by the target radius r. The peak intensity is thus related to the pulse energy $E_\mathcal{P}$ by $I_0 = 2\sqrt{\ln 2}E_\mathcal{P}/r^2\pi^{3/2}\tau_\mathcal{P}$. The chosen parameter values are $\tau_\mathcal{P} = 400$ as and $E_\mathcal{P} = 0.2$ μJ, which is in line with the realistically achievable values for attosecond FEL pulses [31,33], and $\tau_0 = 725$ as is a time offset allowing one to describe the leading tail of the Gaussian pump intensity profile.

Another parameter required by our model is the value of ratio $R_\mathcal{E}$ given by Eq. (16) at which the transition from the correlation-function description to the Maxwell-Bloch equations is performed. For the studied model, we have chosen $R_{\mathcal{E}_i} = 100$ for both fields ($i = 0, 2$) so that the transition between the two sets of equations is performed when the contribution of spontaneous emission on both $K\alpha_{1,2}$ is at least 100 times smaller than that of stimulated emission and thus negligible even if the field gets exponentially amplified. In the following, we will show that choosing this value does not violate the second condition [Eq. (17)].

Figure 2 shows the scaled radiation intensity and number of emitted photons for the two transitions. The $K\alpha_1$ emission exhibits the characteristic features of the different stages of field amplification [8,28,29]. At the beginning of the target, spontaneous emission is the dominant process, and the time profile of the emitted radiation intensity is a convolution of the Gaussian profile of the FEL pump pulse and the exponential decay of the excited state. At larger propagation distances, the emitted field is amplified and the intensity maximum delayed, until the system reaches saturation. Here the delay and duration of the emitted pulse decrease, which is a characteristic sign of superfluorescence, and Rabi oscillations are visible in the temporal profile. The different regimes are also reflected in the number of emitted photons, with a clear progression from an exponential to a linear dependence at a target depth of about 1.5 μm.

The evolution of the field emitted on the $K\alpha_2$ transition is less straightforward and heavily influenced by the stronger $K\alpha_1$ emission. The dependence of the number of emitted $K\alpha_2$ photons is composed of two exponential regions with a change of slope when the $K\alpha_1$ emission reaches saturation. At this point, the population inversion $\rho_{11}(z,\tau) - \rho_{00}(z,\tau)$ becomes negative; however, $\rho_{11}(z,\tau) - \rho_{22}(z,\tau)$ is still positive because the transfer of population to the final state of the $K\alpha_2$ transition is smaller due to the smaller spontaneous decay width. This leads to the second stage of exponential amplification of the $K\alpha_2$ field at propagation distances larger than 1.5 μm.

In the saturation region, the intensity maximum of the $K\alpha_2$ emission follows in time the maximum of the $K\alpha_1$ emission. This is a consequence of the coupling between the two lower states described by ρ_{02}, which is shown in Fig. 3(a). In the scope of the Maxwell-Bloch equations, the evolution of the field emitted on the $1 \to i$ transition is determined by the corresponding density matrix element ρ_{1i}. The significance of ρ_{02} in the evolution of ρ_{1i} can be assessed by looking at the ratios R_i defined by Eqs. (17). While in the case of the $K\alpha_1$ emission (described by ρ_{10} and R_0) the contribution of ρ_{02} is negligible with respect to the population inversion, the evolution of the $K\alpha_2$ emission (described by ρ_{12} and R_2) is mainly determined by the coupling between the lower states [Fig. 3(b)]. Proper modeling of this coupling is thus crucial for the description of field propagation is such systems.

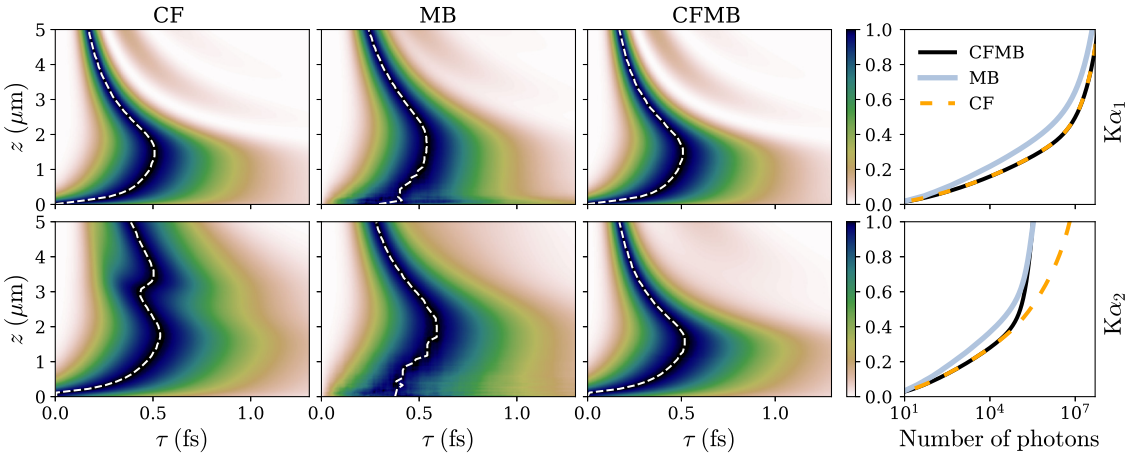

FIG. 4. Intensity of the radiation emitted on the $K\alpha_1$ (top row) and $K\alpha_2$ (bottom row) transitions normalized to the maximum intensity at each propagation distance z for the CF (first column), MB (second column), and CFMB (third column) models, along with the number of emitted photons on each transition for the three models, $\rho_i = 0.08$. The dashed white lines show the position of the intensity maximum.

To check whether taking the initial value of $\rho_{02}(z, \tau)$ in the Maxwell-Bloch equations to be zero is a good approximation, this coherence can be estimated from the propagated quantum correlation functions. Even though Eqs. (12) do not strictly hold at short times and propagation distances, at which spontaneous emission is the dominant process, the fields and coherences can still roughly be estimated using this factorization. Merging the obtained estimates with the fields $\mathcal{E}_{0,2}$ and coherences ρ_{01} and ρ_{21} calculated with the Maxwell-Bloch equations allows for the evaluation of Eq. (13e) in the whole propagation region, leading to the estimated value of ρ_{02} shown on the right side of Fig. 3(a). The figure shows that the agreement between the calculated and estimated values is reasonable and the magnitude of the estimated ρ_{02} is negligible in the transient region between the two sets of equations (denoted by the dashed line); thus the above approximation is justified.

By performing the transition between the two sets of equations when the smaller of the ratios $R_{\mathcal{E}_0,\mathcal{E}_2}$ is equal to a chosen large value, in our case 100, the first condition described at the end of Sec. II is automatically satisfied. The second condition is related to the ratios $R_{0,2}$ defined by Eqs. (17). Figure 3(b) shows that both of these ratios are smaller than 0.1 along the chosen transient line, meaning that also the second condition is satisfied.

B. Comparison of different models of collective x-ray emission

To highlight the differences between the methods generally used to simulate collective emission processes in the x-ray region, we compare three different models. The first is the description of the problem with quantum correlation-function (CF) equations (6), where coupling between the two lower states of the system has been neglected (to be referred to as the CF model). The second is the modeling by means of the semiclassical Maxwell-Bloch (MB) equations (13) with an additional stochastic noise term designed to mimic the effects of spontaneous emission (the MB model) [8,27,28]. This term is included on the right-hand side of Eqs. (13c) and (13d) and is usually modeled as a Gaussian white noise with the following correlation function:

$$\langle f(z_1, \tau_1) f^*(z_2, \tau_2)\rangle = \mathcal{F}\rho_{11}(z_1, \tau_1)\delta(z_1 - z_2)\delta(\tau_1 - \tau_2). \quad (18)$$

The constant factor $\mathcal{F}$ is chosen so as to reproduce the expected number of emitted photons in the spontaneous emission limit. The last model is the combination of correlation-function equations and Maxwell-Bloch equations described in the preceding section (the CFMB model).

In order to simplify the comparison, we neglect the pumping by an external field and assume that at $\tau = 0$, the target is prepared so that the population of the excited state $\rho_{11}(z, 0)$ is equal to some constant value ρ_i throughout the target. Figure 4 shows the scaled intensity and number of photons emitted on the $K\alpha_{1,2}$ transitions calculated with the three models for $\rho_i = 0.08$. In $K\alpha_1$ emission, there is no visible difference between the CF and CFMB models in both the temporal profiles of the emitted field and the number of photons. In the initial part of the target, when spontaneous emission is the dominant process, the intensity maximum is positioned at $\tau = 0$, as expected of the instantaneous swept pumping. However, the results are significantly different in the case of the MB model. The emitted pulse is delayed even at the beginning of the target, clearly showing a shortcoming of modeling spontaneous emission by means of the stochastic noise term. This affects the evolution of the field throughout the target, making the oscillations in the saturation region less pronounced. In the initial part of the target, random fluctuations are visible in the temporal intensity profiles, which are a consequence of averaging the simulation results over a finite number of realizations of the propagation (the MB model results shown in Fig. 4 were averaged over 100 repetitions of the simulation).

The results for the $K\alpha_2$ emission clearly show the advantages of the CFMB method. In the initial part of the target, the system evolution is described by the correlation-function equations (6), so the emitted field profile is similar to the one calculated with the CF model. At larger propagation distances,

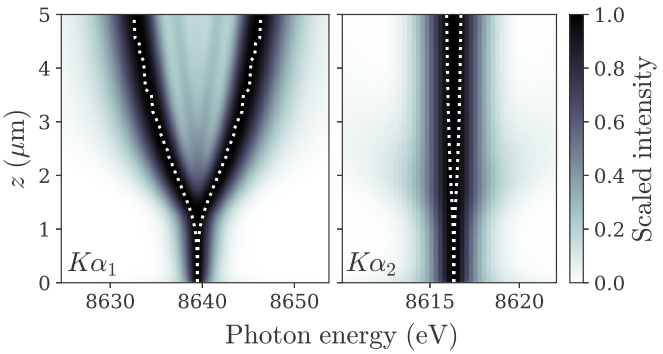

FIG. 5. Spectral intensity of the $K\alpha_1$ (left) and $K\alpha_2$ (right) emission normalized to the maximum intensity at each propagation distance z for $E_{\mathcal{P}} = 0.2$ μJ. The white dotted lines denote $\Omega_{1i} \pm \Omega_{R,i}/2$, where Ω_{1i} $(i = 0, 2)$ is the transition energy and $\Omega_{R,i}$ is the corresponding effective Rabi frequency.

when the emitted fields are amplified, the transition to the Maxwell-Bloch equations (13) is performed and significant differences are noticeable between the results of the CF and CFMB models. In this region, the field evolution is more in line with the MB model, where the peak of $K\alpha_2$ emission also follows in time that of the $K\alpha_1$ emission. The difference between the solutions is also visible in the dependence of the number of emitted photons, with the CF model predicting a much higher number of emitted photons at the end of the target than the other two models.

C. Spectral properties of superfluorescence

Since the lifetimes of core-hole states are on the order of femtoseconds and the duration of x-ray pulses emitted by these states becomes even shorter due to superfluorescence, the intensity profile of the emitted pulses cannot be directly measured in the time domain. The interesting information the developed model can provide is thus the spectral distribution of outgoing radiation, where the different collective emission processes imprint different characteristic features to the spectra.

The evolution of the emitted field spectra throughout the target is shown in Fig. 5, where the pump pulse energy of 0.2 μJ is the same as in the simulations presented in Fig. 2. In the amplification region of $K\alpha_1$ emission in the initial part of the target, the width of the spectral line is similar to the spontaneous emission width due to a similar pulse duration. At a propagation distance of about 1.5 μm, a splitting appears in the $K\alpha_1$ emission spectrum, which is a consequence of the Autler-Townes effect [22]. The predicted characteristic energy splitting of the doublet in the case of the resonant fields is equal to the Rabi frequency, defined as the product of the field amplitude and the corresponding transition dipole moment. Since in our case the field amplitude is time dependent, an effective Rabi frequency can be estimated from the average field amplitude of the emitted pulse as $\Omega_{R,i}(z) = \mu_{i1} \int_0^T |\mathcal{E}_i(z, \tau)| d\tau / T$, where T is the temporal position of the first field intensity minimum. The splitting calculated from the effective Rabi frequency is denoted by white dashed lines in Fig. 5. The two-peaked spectral structure becomes visible when the effective Rabi frequency becomes larger than the spontaneous emission width. Practically no splitting is present in the $K\alpha_2$ emission line due to the lower radiation intensity.

The described shape of the emission lines is a consequence of the time-dependent radiation intensities. In the case of a continuous-wave driving field, the expected shape of the $K\alpha_1$ emission line would be that of a Mollow triplet [44] due to the large intensity of the resonant field coupling states $1s^{-1}$ and $2p_{3/2}^{-1}$. The weaker $K\alpha_2$ field would act as a probe of the field-induced splitting of the common excited state, leading to a two-peaked structure [23]. However, when the coupling is pulsed and the number of field cycles during the pulse duration is small, the dressed-atom picture predicting the described spectral features breaks down [45]. In this case the system evolution can be treated, for example, with Bloch equations, which show that both the number of peaks in the emission spectra and their shapes depend on the coupling pulse properties in a complex way [45–47]. The multipeak structure of the emission spectra is a consequence of the interference of radiation emitted by an atom at different times during the interaction.

Until now we have assumed that the spatial intensity profile of the FEL pulse is uniform; however, realistic sources typically produce pulses with a lateral intensity profile resembling an axially symmetric Gaussian. Moreover, the lateral dimensions of the pump pulse often lead to the case of $F > 1$ (as discussed in Sec. II), leading to non-negligible diffraction effects. Such a situation cannot be accurately modeled in the scope of the developed model. It can however be approximately accounted for by decomposing the target region into smaller extended cylinders characterized by $F = 1$. The radius of each cylinder $r \sim (l^2\lambda^2)^{1/4}$ is given by taking the geometrical solid angle equal to the diffraction solid angle. For each cylinder, the spatial intensity profile of the pump pulse is taken to be uniform, with the corresponding intensities normalized so that the sum of the number of pump photons in each cylinder is equal to the number of pump photons in a pulse with a Gaussian spatial intensity profile featuring a FWHM of $2r_0$ and maximum intensity $I_0 = E_{\mathcal{P}} 2\ln(2)^{3/2}/\tau_{\mathcal{P}} r_0^2 \pi^{3/2}$.

The emission spectra for different pump pulse energies resulting from such spatial averaging for $r_0 = 100$ nm are shown in Fig. 6. The splitting in the $K\alpha_1$ emission line is still clearly discernible in the spatially averaged profiles; however, the dip between the two peaks is less pronounced. This is due to the contributions of regions with smaller pump pulse intensities, where the effective Rabi frequency and separation between the two peaks are smaller. The intensity of the $K\alpha_2$ emission line is about an order of magnitude smaller and again does not exhibit a considerable splitting.

Increasing the pump pulse energy even further could also lead to a splitting of the $K\alpha_2$ emission line; however, this case cannot be accurately simulated with the presented model, as it assumes that the two emitted field modes do not overlap in the spectral domain. Such a situation could lead to modified dynamics due to the field emitted on one transition leading to stimulated emission on the other transition.

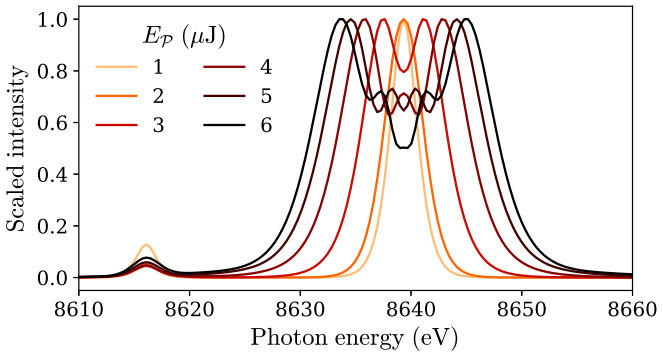

FIG. 6. Spectral intensity of the radiation emitted from a 5-μm-long target on the $K\alpha_1$ (~8639 eV) and $K\alpha_2$ transitions (~8616 eV) at different pump pulse energies. The spatial intensity profile of the pump pulse is assumed to be an axially symmetric Gaussian (see the text). At each pump energy the spectra of the two fields are normalized to the maximum intensity of the $K\alpha_1$ line.

D. Impact of pump pulse duration on the emission spectral line shape

Below we investigate the impact of the pump pulse duration on the predicted self-induced splitting of the $K\alpha_1$ emission line. When the duration of the pump pulse is considerably longer than the lifetime of the excited state, the developed CFMB model does not perform optimally. Namely, the singular-value decomposition used to obtain the initial and boundary conditions for the propagation of Maxwell-Bloch equations yields several singular values with comparable magnitudes corresponding to different incoherent field modes. However, in this case, modeling the evolution by means of the Maxwell-Bloch equations with the stochastic noise term (the MB model; see Sec. III B) yields satisfactory results, as the delay produced by this term is much shorter than the pump pulse duration. For simplicity, the spatial intensity profile of the FEL pulse is taken to be uniform inside a cylinder with radius $r = 28$ nm. Increasing the duration of the pump pulse while keeping the pump pulse energy constant would lead to a decreasing peak pump intensity and consequently a smaller population transfer to the excited state [8]. The intensity of the emitted radiation and the effective Rabi frequency would hence also be smaller, leading to the disappearance of the emission line splitting. It is thus more interesting to study the effect of pump pulse duration while maintaining a constant maximum pump intensity I_0. The results in this section are calculated with $I_0 = 2 \times 10^{19}$ W/cm^2.

Figure 7(a) shows the spectral intensity of the $K\alpha_{1,2}$ emission for varying ratios $\tau_\mathcal{P}/\tau_K$, where $\tau_\mathcal{P}$ is the pump pulse duration and $\tau_K = 400$ as the lifetime of the $1s^{-1}$ core-hole state in zinc. The two-peaked structure of the $K\alpha_1$ emission line cannot be discerned anymore at $\tau_\mathcal{P}/\tau_K = 2$, even though the emitted field reaches saturation even at larger $\tau_\mathcal{P}/\tau_K$ ratios, as can be seen from Fig. 7(b). At long pump pulse duration, strong depopulation of the excited state while the population inversion is still being created leads to a longer duration of the emitted pulses [Fig. 7(b)] and with that narrower emission lines on both transitions. From the results of the preceding

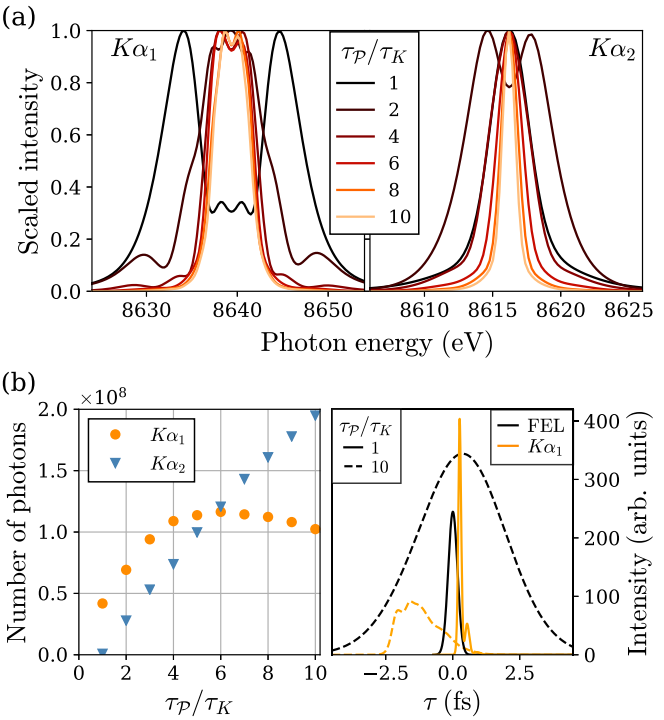

FIG. 7. (a) Scaled spectral intensity of $K\alpha_1$ (left) and $K\alpha_2$ (right) emission emitted from a 5-μm-long target for different $\tau_\mathcal{P}/\tau_K$ ratios. (b) Number of emitted photons as a function of the $\tau_\mathcal{P}/\tau_K$ ratio (left) and temporal intensity profiles of the transmitted FEL pulse and the emitted $K\alpha_1$ field at the end of the target (right).

section, one might anticipate that increasing the maximum pump intensity could lead to the appearance of the emission line splitting even at longer pump pulse durations. However, the simulation results show that this is not the case. Increasing the pump pulse energy to the maximum values achievable with present-day FELs leads to some modifications of the emission line shapes, but no significant splitting is observed.

An interesting consequence of the modified system dynamics at large values of $\tau_\mathcal{P}/\tau_K$ is that the number of photons emitted on the $K\alpha_2$ transition can become significantly larger than that on the $K\alpha_1$, despite the smaller spontaneous decay width. By increasing the pump pulse duration at a constant maximum intensity, the pump pulse energy is effectively increased and with that the density of excited ionic states in the target. As a consequence, the stronger $K\alpha_1$ emission reaches saturation at shorter propagation distances. The rate of depletion of the excited-state population is much smaller in this linear regime, leading to a considerable population inversion on the $K\alpha_2$ transition at longer propagation distances and with that a stronger amplification of the $K\alpha_2$ emission.

The short pump pulse duration with respect to the excited-state lifetime is thus crucial for the observation of the splitting in the emission spectra. As shown in Sec. III C, taking into account the nonuniform spatial intensity profile of the FEL pulse leads to a less pronounced two-peaked spectrum. The splitting would thus become indiscernible at even smaller $\tau_\mathcal{P}/\tau_K$ ratios with respect to the results of Fig. 7. This behavior

is in agreement with the observed amplified $K\alpha$ emission spectra in copper [18], where the FWHM pump pulse duration was 7 fs, much longer than the excited-state lifetime of 0.43 fs [19]. No splitting of the $K\alpha_1$ emission line was observed after reaching saturation; however, at large pump intensities, an asymmetric broadening of the $K\alpha_1$ emission line on the lower-energy side was observed. This seems to be in disagreement with the results of Fig. 7(a). Note, however, that our model does not include the presence of the $3d$ vacancies, which this broadening has been attributed to.

IV. CONCLUSION

We have presented a theoretical approach to modeling collective emission processes in three-level systems, based on a combination of equations for the quantum correlation functions and Maxwell-Bloch equations. Due to the two-part structure, the developed model provides an adequate treatment of both spontaneous emission and coupling of states in strong electric fields. The inclusion of incoherent processes, such as space- and time-dependent pumping and depletion of state populations due to nonradiative decays and photoionization, makes the model suitable for treating collective effects in the x-ray regime.

As an application of the model, we presented numerical results for the evolution of superfluorescence in $K\alpha$ emission in zinc. The calculations predict a clear splitting of the amplified $K\alpha_1$ emission line after reaching saturation, which could be observed with the present-day resolution of x-ray spectrometers. The self-induced splitting has been theoretically predicted before and has been observed in the optical regime, however it has not been experimentally observed in the x-ray domain. The simulations show that the crucial parameter for a clear manifestation of this effect is the duration of the pump pulses, which should be roughly equal to or smaller than the lifetime of the excited state. Realization of such an experiment in the x-ray domain, where the lifetimes of core-hole states are below 1 fs, has only recently become feasible with the demonstration of attosecond FEL sources.

While accounting for incoherent processes concerning the ionic states of the three-level system, the developed model does not take into account other processes, possibly induced by the high-intensity pump pulses, such as production of the $3d$ vacancies via shake processes [30], shifts of the energy levels induced by the changed ionization states of neighboring atoms, and sequential multistage pumping processes [48]. These could lead to additional spectral intensity and a change of the emission line shape. Experimental observation is thus crucial for the evaluation of the presented results and further development of the theoretical model.

ACKNOWLEDGMENTS

This work was supported by the Slovenian Research Agency Program No. P1-0112 and Project No. J1-8134. The authors acknowledge the essential contribution of the Network Infrastructure Centre of Jožef Stefan Institute operating the NSC computing cluster, on which the calculations were performed.

APPENDIX A: EFFECT OF MAGNETIC SUBSTRUCTURE OF THE IONIC STATES AND POLARIZATION PROPERTIES OF THE EMITTED FIELD

After photoionization by the FEL pulse, the two excited vacancy states $|1s_{1/2,1/2}\rangle$ and $|1s_{1/2,-1/2}\rangle$ are equally populated. We assume that the pump field is linearly polarized and z is the quantization axis. Let us consider $K\alpha_2$ transitions to states $|2p_{1/2,1/2}\rangle$ and $|2p_{1/2,-1/2}\rangle$. The matrix elements of the ionic dipole operator $\hat{\boldsymbol{D}} = (\hat{D}_x, \hat{D}_y, \hat{D}_z)$ in the chosen coordinate system can be calculated by applying the Wigner-Eckart theorem. For transitions between the four different pairs of states these are

$$\begin{aligned}\boldsymbol{\mu}_1 &= \langle 2p_{1/2,1/2}|\hat{\boldsymbol{D}}|1s_{1/2,1/2}\rangle \\ &= \frac{1}{\sqrt{6}}(0,0,-1)\langle 1/2||D||1/2\rangle, \qquad \text{(A1a)}\\ \boldsymbol{\mu}_2 &= \langle 2p_{1/2,-1/2}|\hat{\boldsymbol{D}}|1s_{1/2,-1/2}\rangle \\ &= \frac{1}{\sqrt{6}}(0,0,1)\langle 1/2||D||1/2\rangle, \qquad \text{(A1b)}\\ \boldsymbol{\mu}_3 &= \langle 2p_{1/2,-1/2}|\hat{\boldsymbol{D}}|1s_{1/2,1/2}\rangle \\ &= \frac{1}{\sqrt{3}}\left(\frac{1}{\sqrt{2}}, \frac{i}{\sqrt{2}}, 0\right)\langle 1/2||D||1/2\rangle, \qquad \text{(A1c)}\\ \boldsymbol{\mu}_4 &= \langle 2p_{1/2,1/2}|\hat{\boldsymbol{D}}|1s_{1/2,-1/2}\rangle \\ &= \frac{1}{\sqrt{3}}\left(\frac{1}{\sqrt{2}}, -\frac{i}{\sqrt{2}}, 0\right)\langle 1/2||D||1/2\rangle, \qquad \text{(A1d)}\end{aligned}$$

where $\langle j_f||D||j_i\rangle$ is the reduced dipole matrix element. The corresponding angular distributions of emitted photons are proportional to

$$\frac{d\sigma_1}{d\Omega} = \frac{3}{8\pi}\sin^2\theta\frac{|\langle 1/2||D||1/2\rangle|^2}{6}, \qquad \text{(A2a)}$$

$$\frac{d\sigma_2}{d\Omega} = \frac{3}{8\pi}\sin^2\theta\frac{|\langle 1/2||D||1/2\rangle|^2}{6}, \qquad \text{(A2b)}$$

$$\frac{d\sigma_3}{d\Omega} = \frac{3}{32\pi}(3+\cos 2\theta - 2\sin^2\theta\sin 2\phi)\frac{|\langle 1/2||D||1/2\rangle|^2}{3}, \qquad \text{(A2c)}$$

$$\frac{d\sigma_4}{d\Omega} = \frac{3}{32\pi}(3+\cos 2\theta + 2\sin^2\theta\sin 2\phi)\frac{|\langle 1/2||D||1/2\rangle|^2}{3}, \qquad \text{(A2d)}$$

where θ and ϕ are the azimuthal and polar angles in the chosen coordinate system, respectively. Summing over all contributions shows that the joint angular distribution is isotropic, $d\sigma/d\Omega = |\langle 1/2||D||1/2\rangle|^2/4\pi$.

In the case of extended targets, the active medium interacts with photons emitted along the propagation direction of the pump field. Inserting $\theta = \pi/2$ and $\phi = 0$ into the above angular distributions shows that in each of the four transitions an equal number of photons is emitted in the forward direction. Photons emitted in the first two transitions are polarized along the polarization of the pump field, whereas the polarization of photons emitted in the last two transitions is orthogonal to the polarization of the pump field and the propagation direction. Each of the initial states $|1s_{1/2,1/2}\rangle$ and $|1s_{1/2,-1/2}\rangle$ thus contributes an equal number of photons to each of the

polarization modes in the forward direction. A similar analysis can be performed for the $K\alpha_1$ transitions, leading to the same conclusion, though with twice the number of emitted photons.

In the following we show that the magnetic substructure and polarization properties can also be neglected in the case of stimulated emission. To this end we consider two models of $K\alpha_2$ emission. The target is modeled as a sequence of layers with width Δz, where each of the layers undergoes the same time evolution modeled in time steps $\Delta t = \Delta z/c$. In the first model, which encompasses the magnetic substructure of the ionic levels and polarization properties of the emitted light, the initially equally populated excited states $|1s_{1/2,1/2}\rangle$ and $|1s_{1/2,-1/2}\rangle$ decay by emission of photons with one of two different polarizations $|H\rangle$ and $|V\rangle$ with the spontaneous decay rate independent of the magnetic quantum number of the initial and final ionic states. At each time step, $n+1$ photons are emitted from a layer of atoms, where n is the total number of photons in the previous time step and target layer. This takes into account both spontaneous and stimulated emission, where the probability for emission of photons with a certain polarization is proportional to the number of photons with that same polarization entering the target layer. The polarization of the spontaneously emitted photon and the excited state, from which each of the $n+1$ photons is emitted, is randomly chosen. The obtained results are compared to a simplified model, where photons, all with the same polarization $|S\rangle$, are emitted in the transition from a single excited state $|1\rangle$ to a single final state $|2\rangle$. The decay rate for $|1\rangle \rightarrow |2\rangle$ spontaneous transition is the same as above and the population of each of the two states $|1\rangle$ and $|2\rangle$ is considered equal to the sum of the populations of the corresponding physical states over the magnetic quantum numbers.

The results obtained with the two models of $K\alpha_2$ emission are presented in Fig. 8. The bottom panel of the figure shows that on average the sum of the populations of the two excited states $|1s_{1/2,1/2}\rangle$ and $|1s_{1/2,-1/2}\rangle$ of the first model coincides with the population of the single excited state $|1\rangle$ of the second model at all times. Similarly, the sum of the emitted photons with polarizations $|H\rangle$ and $|V\rangle$ in the first model is on average equal to the number of emitted photons in the second model. This shows that the simplified model, which omits the magnetic substructure of the ionic levels and polarization properties of the emitted light, adequately describes the $K\alpha_{1,2}$ decay even in the case of stimulated emission. In principle, when propagating the equations, any of the two initial magnetic substates can be taken as $|1\rangle$ and any of the two final magnetic substates can be taken as $|2\rangle$. The correspondence $|1s_{1/2,1/2}\rangle \rightarrow |1\rangle$ and $|2p_{1/2,1/2}\rangle \rightarrow |2\rangle$ and thus $|S\rangle \rightarrow |V\rangle$ is preferable because the parallelism of the transition dipole moment and photon polarization leads to a simplification of the propagation equations. The magnitude of dipole matrix element equals the magnitude of the reduced dipole matrix element, $\mu_{12} = \langle 1/2||D||1/2\rangle$.

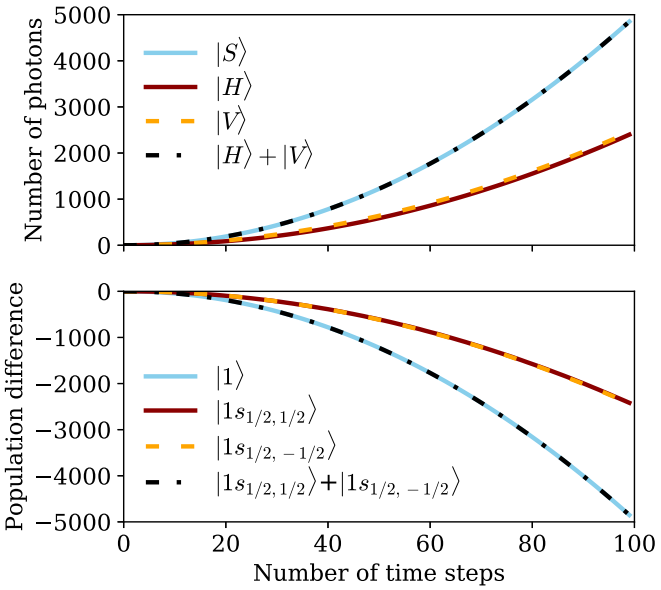

FIG. 8. Shown on top is the number of emitted photons and on bottom the difference in ionic state populations with respect to initial populations for the two $K\alpha_2$ decay models described in the text. The results of the model which considers the magnetic substructure of ionic states and different polarizations are averaged over 20 repetitions of the simulation. The initial population of states $|1s_{1/2,1/2}\rangle$ and $|1s_{1/2,-1/2}\rangle$ is 10^6.

APPENDIX B: DERIVATION OF THE QUANTUM CORRELATION-FUNCTION EQUATIONS FOR A THREE-LEVEL SYSTEM

Below we provide a more detailed description of the derivation of the set of equations (6). Since a complete derivation of an analogous system of equations for a two-level system is presented in Ref. [29], we will here only describe the key points and differences allowing one to obtain a set of equations for a three-level system. All the intermediate missing steps are detailed in Ref. [29].

The Hamiltonian (1) leads to a set of Heisenberg-Langevin equations for transition operators $\hat{\sigma}_{ij}^{(\alpha)}$, $i, j = 0, 1, 2$, and field operators $\hat{a}_{\boldsymbol{k}s}^{(\dagger)}$ and $\hat{b}_{\boldsymbol{q}s}^{(\dagger)}$. The latter can be formally integrated to yield

$$\hat{a}_{\boldsymbol{k},s}(t) = \hat{a}_{\boldsymbol{k},s}(0)e^{-i\omega_{\boldsymbol{k}}t} - i\sum_{\beta} e^{-i\boldsymbol{k}\cdot\boldsymbol{r}_\beta} g^*_{\boldsymbol{k},s} \int_0^t dt' e^{-i\omega_{\boldsymbol{k}}(t-t')}\hat{\sigma}_{01}^{(\beta)}(t'), \quad \text{(B1a)}$$

$$\hat{b}_{\boldsymbol{q},s}(t) = \hat{b}_{\boldsymbol{q},s}(0)e^{-i\omega_{\boldsymbol{q}}t} - i\sum_{\beta} e^{-i\boldsymbol{q}\cdot\boldsymbol{r}_\beta} d^*_{\boldsymbol{q},s} \int_0^t dt' e^{-i\omega_{\boldsymbol{q}}(t-t')}\hat{\sigma}_{21}^{(\beta)}(t'), \quad \text{(B1b)}$$

which are then substituted into the equations for operators $\hat{\sigma}_{ij}^{(\alpha)}$. The sums over all atoms of the system $\sum_\beta$ can be split into two parts: $\beta = \alpha$ results in terms proportional to the spontaneous decay width, whereas the sum over $\beta \neq \alpha$ describes the interaction of a given atom with all other atoms. Defining the spontaneous decay widths as

$$\Gamma_i^{sp} = \frac{|\boldsymbol{\mu}_{1i}|^2\Omega_{1i}^3}{3\pi\hbar\epsilon_0 c^3}, \quad i = 0, 2 \quad \text{(B2)}$$

and the electric field modes as

$$\hat{\mathcal{E}}^{(\alpha)}_{0,+}(t) = -i\sum_{\beta\neq\alpha}\sum_{\boldsymbol{k},s}\boldsymbol{e}_{\boldsymbol{k},s}\sqrt{\frac{\hbar\omega_{\boldsymbol{k}}}{2\epsilon_0 V}}g^{*}_{\boldsymbol{k},s}e^{i\boldsymbol{k}\cdot(\boldsymbol{r}_\alpha-\boldsymbol{r}_\beta)} \times\int_0^t dt' e^{-i\omega_{\boldsymbol{k}}(t-t')}\hat{\sigma}^{(\beta)}_{01}(t'), \tag{B3a}$$

$$\hat{\mathcal{E}}^{(\alpha)}_{2,+}(t) = -i\sum_{\beta\neq\alpha}\sum_{\boldsymbol{q},s}\boldsymbol{e}_{\boldsymbol{q},s}\sqrt{\frac{\hbar\omega_{\boldsymbol{q}}}{2\epsilon_0 V}}d^{*}_{\boldsymbol{q},s}e^{i\boldsymbol{q}\cdot(\boldsymbol{r}_\alpha-\boldsymbol{r}_\beta)} \times\int_0^t dt' e^{-i\omega_{\boldsymbol{q}}(t-t')}\hat{\sigma}^{(\beta)}_{21}(t') \tag{B3b}$$

leads to the following set of equations for the time propagation of transition operators:

$$\dot{\hat{\sigma}}^{(\alpha)}_{00} = \Gamma^{\mathrm{sp}}_0\hat{\sigma}^{(\alpha)}_{11} + \frac{i}{\hbar}(\hat{\sigma}^{(\alpha)}_{10}\boldsymbol{\mu}_{10}\cdot\hat{\boldsymbol{\mathcal{E}}}^{(\alpha)}_{0,+} - \boldsymbol{\mu}_{01}\cdot\hat{\boldsymbol{\mathcal{E}}}^{(\alpha)}_{0,-}\hat{\sigma}^{(\alpha)}_{01}) + F^{(\alpha)}_{00}, \tag{B4a}$$

$$\dot{\hat{\sigma}}^{(\alpha)}_{11} = -(\Gamma^{\mathrm{sp}}_0+\Gamma^{\mathrm{sp}}_2)\hat{\sigma}^{(\alpha)}_{11} - \frac{i}{\hbar}(\hat{\sigma}^{(\alpha)}_{10}\boldsymbol{\mu}_{10}\cdot\hat{\boldsymbol{\mathcal{E}}}^{(\alpha)}_{0,+} - \boldsymbol{\mu}_{01}\cdot\hat{\boldsymbol{\mathcal{E}}}^{(\alpha)}_{0,-}\hat{\sigma}^{(\alpha)}_{01} + \hat{\sigma}^{(\alpha)}_{12}\boldsymbol{\mu}_{12}\cdot\hat{\boldsymbol{\mathcal{E}}}^{(\alpha)}_{2,+} - \boldsymbol{\mu}_{21}\cdot\hat{\boldsymbol{\mathcal{E}}}^{(\alpha)}_{2,-}\hat{\sigma}^{(\alpha)}_{21}) + F^{(\alpha)}_{11}, \tag{B4b}$$

$$\dot{\hat{\sigma}}^{(\alpha)}_{22} = \Gamma^{\mathrm{sp}}_2\hat{\sigma}^{(\alpha)}_{11} + \frac{i}{\hbar}(\hat{\sigma}^{(\alpha)}_{12}\boldsymbol{\mu}_{12}\cdot\hat{\boldsymbol{\mathcal{E}}}^{(\alpha)}_{2,+} - \boldsymbol{\mu}_{21}\cdot\hat{\boldsymbol{\mathcal{E}}}^{(\alpha)}_{2,-}\hat{\sigma}^{(\alpha)}_{21}) + F^{(\alpha)}_{22}, \tag{B4c}$$

$$\dot{\hat{\sigma}}^{(\alpha)}_{01} = -\left(i\Omega_{10}+\frac{\Gamma^{\mathrm{sp}}_0+\Gamma^{\mathrm{sp}}_2}{2}\right)\hat{\sigma}^{(\alpha)}_{01} + \frac{i}{\hbar}(\hat{\sigma}^{(\alpha)}_{11}-\hat{\sigma}^{(\alpha)}_{00}) \times\boldsymbol{\mu}_{10}\cdot\hat{\boldsymbol{\mathcal{E}}}^{(\alpha)}_{0,+} - \frac{i}{\hbar}\hat{\sigma}^{(\alpha)}_{02}\boldsymbol{\mu}_{12}\cdot\hat{\boldsymbol{\mathcal{E}}}^{(\alpha)}_{2,+} + F^{(\alpha)}_{01}, \tag{B4d}$$

$$\dot{\hat{\sigma}}^{(\alpha)}_{21} = -\left(i\Omega_{12}+\frac{\Gamma^{\mathrm{sp}}_0+\Gamma^{\mathrm{sp}}_2}{2}\right)\hat{\sigma}^{(\alpha)}_{21} + \frac{i}{\hbar}(\hat{\sigma}^{(\alpha)}_{11}-\hat{\sigma}^{(\alpha)}_{22}) \times\boldsymbol{\mu}_{12}\cdot\hat{\boldsymbol{\mathcal{E}}}^{(\alpha)}_{2,+} - \frac{i}{\hbar}\hat{\sigma}^{(\alpha)}_{20}\boldsymbol{\mu}_{10}\cdot\hat{\boldsymbol{\mathcal{E}}}^{(\alpha)}_{0,+} + F^{(\alpha)}_{21}, \tag{B4e}$$

$$\dot{\hat{\sigma}}^{(\alpha)}_{20} = i\Omega_{20}\hat{\sigma}^{(\alpha)}_{20} - \frac{i}{\hbar}\boldsymbol{\mu}_{01}\cdot\hat{\boldsymbol{\mathcal{E}}}^{(\alpha)}_{0,-}\hat{\sigma}^{(\alpha)}_{21} + \frac{i}{\hbar}\hat{\sigma}^{(\alpha)}_{10}\boldsymbol{\mu}_{12}\cdot\hat{\boldsymbol{\mathcal{E}}}^{(\alpha)}_{2,+} + F^{(\alpha)}_{20}. \tag{B4f}$$

Here $\Omega_{ij} = (E_i - E_j)/\hbar$ are the transition energies and $F^{(\alpha)}_{ij}$ correspond to the stochastic Langevin operators, as they include the values of the field operators at the initial time $\hat{a}^{(\dagger)}_{\boldsymbol{k}s}(0)$ and $\hat{b}^{(\dagger)}_{\boldsymbol{q}s}(0)$, when these are in a vacuum state.

Since the excited part of the medium has the shape of an elongated cylinder, we can assume that only the field modes with wave vectors oriented within a small solid angle Δo around the cylinder axis z will interact with a large number of excited atoms and will thus be amplified. We also assume that the vectors of the dipole transition matrix elements are oriented along the polarization direction of the induced fields. The sum over wave vectors in Eqs. (B3) can thus be replaced with

$$\int d^3\boldsymbol{k} \to \Delta o\int_0^\infty\frac{\omega^2}{c^3}d\omega \tag{B5}$$

and a similar expression for the integration over the wave vector $\boldsymbol{q}$. With this the induced field operators can be expressed as

$$\hat{\mathcal{E}}^{(\alpha)}_{i,+}(\tau) = -\frac{i\Delta o\mu_{i1}\Omega^3_{1i}}{16\pi^2\epsilon_0 c^2}\sum_{\beta<\alpha}\hat{\sigma}^{(\beta)}_{i1}(\tau), \tag{B6}$$

where the retarded time τ is defined for each atom α as $\tau = t - z_\alpha/c$ and $i = 0, 2$.

Inserting these expressions into Eqs. (B4) leads to a closed set of equations for the transition operators $\hat{\sigma}_{ij}$, which can be used to obtain the equations for the expectation values of state populations, correlation functions of atomic coherences, and field correlation functions following the procedure described in Ref. [29]. In this derivation we made the approximation described in Sec. II, i.e., we neglected the terms in equations for the atomic correlation functions which contain operators $\hat{\sigma}_{02,20}$. Equation (B4f) directly shows that these contributions are small when the electric fields are weak.

Maxwell-Bloch equations for the density matrix elements can be obtained from Eqs. (B4) by neglecting the stochastic Langevin terms $\hat{F}^{(\alpha)}_{ij}$, replacing the operators with complex numbers and introducing continuous variables in an analogous way as in Eq. (7). Making the replacement $\hat{\sigma}_{i1}\to\rho_{1i}$ and $\sum_{\beta<\alpha}\to\int_0^z dz$ in Eqs. (B3) and differentiating the obtained expressions with respect to z also leads to the propagation equations for the electric fields, which contain the geometrical factor ξ defined in Eq. (15).

Incoherent processes are modeled by including Lindblad superoperators in the master equations for the density matrix. For details, see Ref. [29].

[1] G. I. Peters and L. Allen, J. Phys. A: Gen. Phys. **4**, 238 (1971).
[2] L. Allen and G. I. Peters, J. Phys. A: Gen. Phys. **4**, 564 (1971).
[3] M. Gross and S. Haroche, Phys. Rep. **93**, 301 (1982).
[4] U. Ganiel, A. Hardy, G. Neumann, and D. Treves, IEEE J. Quantum Electron. **11**, 881 (1975).
[5] S. R. Wilk, R. W. Boyd, and K. J. Teegarden, Opt. Commun. **47**, 404 (1983).
[6] N. Skribanowitz, I. P. Herman, J. C. MacGillivray, and M. S. Feld, Phys. Rev. Lett. **30**, 309 (1973).
[7] H. M. Gibbs, Q. H. F. Vrehen, and H. M. J. Hikspoors, Phys. Rev. Lett. **39**, 547 (1977).
[8] Š. Krušič, K. Bučar, A. Mihelič, and M. Žitnik, Phys. Rev. A **98**, 013416 (2018).
[9] M. Nagasono, J. R. Harries, H. Iwayama, T. Togashi, K. Tono, M. Yabashi, Y. Senba, H. Ohashi, T. Ishikawa, and E. Shigemasa, Phys. Rev. Lett. **107**, 193603 (2011).
[10] K. Nakajima, J. R. Harries, H. Iwayama, S. Kuma, Y. Miyamoto, M. Nagasono, C. Ohae, T. Togashi, M. Yabashi, E. Shigemasa, and N. Sasao, J. Phys. Soc. Jpn. **84**, 054301 (2015).
[11] M. S. Malcuit, J. J. Maki, D. J. Simkin, and R. W. Boyd, Phys. Rev. Lett. **59**, 1189 (1987).

[12] L. Allen and G. Peters, Phys. Lett. **31A**, 95 (1970).
[13] R. H. Dicke, Phys. Rev. **93**, 99 (1954).
[14] E. Allaria *et al.*, Nat. Photon. **6**, 699 (2012).
[15] P. Emma *et al.*, Nat. Photon. **4**, 641 (2010).
[16] D. Pile, Nat. Photon. **5**, 456 (2011).
[17] N. Rohringer, D. Ryan, R. A. London, M. Purvis, F. Albert, J. Dunn, J. D. Bozek, C. Bostedt, A. Graf, R. Hill, S. P. Hau-Riege, and J. J. Rocca, Nature (London) **481**, 488 (2012).
[18] H. Yoneda, Y. Inubushi, K. Nagamine, Y. Michine, H. Ohashi, H. Yumoto, K. Yamauchi, H. Mimura, H. Kitamura, T. Katayama, T. Ishikawa, and M. Yabashi, Nature (London) **524**, 446 (2015).
[19] M. O. Krause and J. H. Oliver, J. Phys. Chem. Ref. Data **8**, 329 (1979).
[20] T. Kroll, C. Weninger, R. Alonso-Mori, D. Sokaras, D. Zhu, L. Mercadier, V. P. Majety, A. Marinelli, A. Lutman, M. W. Guetg *et al.*, Phys. Rev. Lett. **120**, 133203 (2018).
[21] L. Mercadier, A. Benediktovitch, C. Weninger, M. A. Blessenohl, S. Bernitt, H. Bekker, S. Dobrodey, A. Sanchez-Gonzalez, B. Erk, C. Bomme *et al.*, Phys. Rev. Lett. **123**, 023201 (2019).
[22] S. H. Autler and C. H. Townes, Phys. Rev. **100**, 703 (1955).
[23] C. N. Cohen-Tannoudji, *Amazing Light* (Springer, Berlin, 1996), pp. 109–123.
[24] T. E. Glover, M. P. Hertlein, S. H. Southworth, T. K. Allison, J. van Tilborg, E. P. Kanter, B. Krässig, H. R. Varma, B. Rude, R. Santra, A. Belkacem, and L. Young, Nat. Phys. **6**, 69 (2010).
[25] M. Žitnik, A. Mihelič, K. Bučar, M. Hrast, Ž. Barba, Š. Krušič, P. Rebernik Ribič, J. Urbančič, B. Ressel, M. Stupar, L. Poletto, M. Coreno, D. Gauthier, and G. De Ninno, Phys. Rev. A **99**, 053423 (2019).
[26] P. D. Drummond and M. G. Raymer, Phys. Rev. A **44**, 2072 (1991).
[27] O. Larroche, D. Ros, A. Klisnick, A. Sureau, C. Möller, and H. Guennou, Phys. Rev. A **62**, 043815 (2000).
[28] C. Weninger and N. Rohringer, Phys. Rev. A **90**, 063828 (2014).
[29] A. Benediktovitch, V. P. Majety, and N. Rohringer, Phys. Rev. A **99**, 013839 (2019).
[30] Y. Ito, T. Tochio, H. Ohashi, M. Yamashita, S. Fukushima, M. Polasik, K. Słabkowska, L. Syrocki, E. Szymańska, J. Rzadkiewicz, P. Indelicato, J. P. Marques, M. C. Martins, J. P. Santos, and F. Parente, Phys. Rev. A **94**, 042506 (2016).
[31] S. Huang, Y. Ding, Y. Feng, E. Hemsing, Z. Huang, J. Krzywinski, A. A. Lutman, A. Marinelli, T. J. Maxwell, and D. Zhu, Phys. Rev. Lett. **119**, 154801 (2017).
[32] A. Marinelli, J. MacArthur, P. Emma, M. Guetg, C. Field, D. Kharakh, A. A. Lutman, Y. Ding, and Z. Huang, Appl. Phys. Lett. **111**, 151101 (2017).
[33] J. Duris *et al.*, Nat. Photon. **14**, 30 (2020).
[34] Y. Ito, T. Tochio, H. Oohashi, and A. Vlaicu, in *Proceedings of the 20th International Conference on X-Ray and Inner-Shell Processes*, edited by C. T. Chantler, special issue of Radiat. Phys. Chem. **75**, 1534 (2006).
[35] F. Parpia, C. Fischer, and I. Grant, Comput. Phys. Commun. **94**, 249 (1996).
[36] M. O. Scully and M. S. Zubairy, *Quantum Optics* (Cambridge University Press, Cambridge, 1997).
[37] M. Altarelli, in *Magnetism: A Synchrotron Radiation Approach*, edited by E. Beaurepaire, H. Bulou, F. Scheurer, and J.-P. Kappler (Springer, Berlin, 2006), pp. 201–242.
[38] P. Lambropoulos and D. Petrosyan, *Fundamentals of Quantum Optics and Quantum Information* (Springer, Berlin, 2007), Vol. 23 .
[39] H. Yanai, K. Takeuchi, and Y. Takane, *Projection Matrices, Generalized Inverse Matrices, and Singular Value Decomposition* (Springer Science + Business Media, New York, 2011).
[40] M. O. Krause, J. Phys. Chem. Ref. Data **8**, 307 (1979).
[41] A. C. Thompson *et al.*, *X-Ray Data Booklet* (Lawrence Berkeley National Laboratory, University of California, Berkeley, 2001), Vol. 8.
[42] J. H. Scofield, Theoretical photoionization cross sections from 1 to 1500 keV, Lawrence Livermore Laboratory Report No. UCRL-51326, 1973 (unpublished).
[43] S. Fritzsche, in *Proceedings of the Eighth International Conference on Electronic Spectroscopy and Structure*, edited by A. P. Hitchcock and K. T. Leung, special issue of J. Electron Spectrosc. Relat. Phenom. **114–116**, 1155 (2001).
[44] B. R. Mollow, Phys. Rev. **188**, 1969 (1969).
[45] M. Lewenstein, J. Zakrzewski, and K. Rzazewski, J. Opt. Soc. Am. B 3, 22 (1986).
[46] K. Rzazewski and M. Florjanczyk, J. Phys. B **17**, L509 (1984).
[47] M. Florjaczyk, K. Rzązewski, and J. Zakrzewski, Phys. Rev. A **31**, 1558 (1985).
[48] *X-Ray Free Electron Lasers: Applications in Materials, Chemistry and Biology*, edited by U. Bergmann, V. Yachandra, and J. Yano, (Royal Society of Chemistry, Cambridge, 2017).